Journal of Alloys and Compounds 509 (2011) 5127–5136

Contents lists available at ScienceDirect

Journal of Alloys and Compounds

journal homepage: www.elsevier.com/locate/jallcom

Electron spin resonance and resistivity studies of charge-ordered $Bi_{(1-x)}Sr_xMnO_3$

Joji Kurian, R. Singh*

School of Physics, University of Hyderabad, Central University P.O., Hyderabad 500046, India

ARTICLE INFO

Article history:
Received 18 August 2010
Received in revised form 28 January 2011
Accepted 31 January 2011
Available online 1 March 2011

Keywords:
Manganites
Magnetic interactions
Electronic phase separation
ESR
Polaron hopping

ABSTRACT

In this paper we report the temperature dependent electron spin resonance (ESR) and electrical resistivity studies of $Bi_{(1-x)}Sr_xMnO_3$ ($x = 0.3$, 0.4, 0.45, and 0.5). The double integrated (DI) intensity of the ESR signal vs temperature (T) and ln DI vs $1000/T$ plots have been used to get information about magnetic interactions in the sample. A sharp change in the slope of this plot indicates the onset of long range antiferromagnetic (AFM) order. The Neel temperatures (T_N) of the sample increases with increase in Sr content. In the temperature range $T > T_N$, domains of ferromagnetic (FM) and AFM correlations co-exist. The contributions of AFM correlations increase with the increase in Sr content. The observation of weak ESR signal in the temperature range below T_N indicates the freezing of FM microdomains/inhomogeneities in the AFM long range ordered state. The resistivity (ρ) data are analyzed in view of polaron model and variable range hopping (VRH) models given by Mott and Efros–Shklovskii (ES). As per Motts VRH model, ln ρ varies linearly with $T^{-1/4}$ with a change in slope at T_N. The estimated values of hopping distance and localization length are reasonable. It is also found that ln ρ varies linearly with $T^{-1/2}$ in accordance with the ES VRH model. However, the estimated values of the model parameters are unrealistic. The ESR and resistivity data are also analyzed in view of phase separation (PS) model.

1. Introduction

The general formula of the perovskite structure is given as $ABO_{3-\delta}$, where A can be an alkali, alkaline earth or rare-earth ion and B a transition metal ion. The B-site ion is selected to retain desirable properties of the end compound. Based on the Verway controlled ionic valence principle the conduction and hence the carrier concentration of the B-site ions can be controlled by substituting a donor or acceptor at the A-site. A very common element used at the B-site is manganese and the compounds formed are called manganites.

The discovery of the colossal magnetoresistance (CMR) effect in manganites by Jin et al. [1] and Xiong et al. [2] heightened research activity on these materials. Tokura et al. [3] proposed that the charge ordered (CO) state observed by Jirak et al. [4] is vital for explaining the CMR effect. Charge ordering is a phenomenon of exceptional importance in perovskite manganites as it can dictate specific magnetic, transport as well as CMR properties [5]. The Coulomb repulsion between charges and the elastic energy from the static Jahn–Teller (JT) deformations that accommodate the associated orbital ordering (OO) regulate the stability of the CO state. Even though the covalence effects are important, the ionic picture describes CO as a real space ordering of the e_g electrons.

To understand the phenomenon of charge/orbital ordering (CO/OO) is important in view of their implication on the physical properties of manganites. For the half-hole doped manganites, it is expected that the antiferromagnetic (AFM) phase is formed at a lower temperature on cooling a CO/OO state which had already set in at a certain higher temperature [6–8]. The La-based manganites have been extensively studied for their electrical and magnetic properties. Although Bi^{3+} has ionic radius similar to that of La^{3+} the resultant $ABO_{3-\delta}$ materials have very different properties viz. $LaMnO_3$ is an antiferromagnet (AFM) having orthorhombic structure whereas $BiMnO_3$ is a ferromagnet (FM) with triclinic structure [9].

In the recent years Bi based manganites have been studied for their basic properties as well as for applications. $BiMnO_3$ exhibits ferroelectric as well as ferromagnetic properties and hence can be used as a good multiferroic material [10,11]. The Bi doped manganites have been shown to be prospective materials for multiferroic and bolometric applications [12–15]. $Bi_{0.5}Sr_{0.5}MnO_3$ has been shown to be a promising candidate for use as a cathode material in solid oxide fuel cells because of its high electrochemical performance [16].

There have been a number of studies on the $Bi_{(1-x)}Sr_xMnO_3$ (BSMO) system in the recent years. This system is known to have higher charge ordering temperature (T_{CO}) in the range ~500–600 K compared to ~300 K for $Bi_{(1-x)}Ca_xMnO_3$ system for a wide range of x values. The peculiar properties of BSMO system have been attributed to the electronic structure of the Bi^{3+} ions, which have

* Corresponding author. Tel.: +91 40 2313 4321; fax: +91 40 2301 0227.
E-mail address: rssp@uohyd.ernet.in (R. Singh).

0925-8388/$ – see front matter © 2011 Elsevier B.V. All rights reserved.
doi:10.1016/j.jallcom.2011.01.207

highly polarizable $6s^2$ lone pairs responsible for decrease in mobility of the itinerant e_g electrons [17–20]. The magnetic and structural studies on this system by Garcia-Munoz et al. [20] showed the higher stability of CO state in the case of half doped sample. This is attributed to the maximal Coulomb energy gain due to CO and strain energy gain due to OO for Mn^{3+}/Mn^{4+} ratio of 1. The results suggest that the $6s^2$ lone pair of Bi^{3+} is weakly screened in (Bi, Sr) MnO_3 compounds. An orientation of the $6s^2$ lone pair towards a surrounding anion (O^{2-}) can produce local distortion or hybridization between 6s-Bi-orbitals and 2p-O-orbitals, reducing the movement of e_g electrons through the Mn–O–Mn bridges and favouring CO state. The Sr rich $Bi_{(1-x)}Sr_xMnO_3$ system studied by Sedmidubsky et al. [21] shows a gradual decrease of T_{CO} from ~550 K for $x = 0.5$ to almost 0 K at $x = 0.9$. The thermopower in the temperature range $T > T_{CO}$ is constant and characteristic of polaronic transport. Whereas in the temperature range $T < T_{CO}$ an activated transport mechanism of localized charge carriers is observed.

Resonant X-ray scattering at the Mn K edge of $Bi_{0.63}Sr_{0.37}MnO_3$ single crystals carried out by Subias et al. [22] showed the compound undergoing a metal–insulator phase transition to a CO state at ~530 K. These studies agree with a strongly stable checkerboard pattern ordering in the ab plane of manganese atoms in two geometries: one site is anisotropic with tetragonally distorted oxygen octahedron and the other one is isotropic with nearly undistorted oxygen octahedron as observed for half-doped manganites $Bi_{0.5}Sr_{0.5}MnO_3$. Differential scanning calorimetry studies on $Bi_{1-x}Sr_xMnO_3$ were used to examine the transition from the high-temperature pseudocubic form to an orthorhombically distorted CO state by Sedmidubsky et al. [23]. The effect of CO and OO on the magnetic properties of the $Bi_{(1-x)}Sr_xMnO_3$ system was carried out by Mantytskaya et al. [24]. Based on these studies a magnetic phase diagram is provided over a wide range of x values. The high temperature resistivity, susceptibility and thermoelectric power (TEP) measurements are reported by Kim et al. [25] on BSMO system. The susceptibility and resistivity data are reported to follow Curie–Weiss law and polaron variable range hopping (VRH) conduction mechanism respectively. TEP is found to be negative and weakly temperature dependent. The electrical transport properties are interpreted in terms of carrier localization accompanied by the local lattice distortions due to Bi^{3+} lone pairs. A relation between TEP and magnetic susceptibility is also established in ref. [26]. Rebello and Mahendiran [27] have reported pulsed as well as direct current/voltage induced electro resistance in $Bi_{0.8}Sr_{0.2}MnO_3$ at room temperature. They observed that bi-level and multilevel resistivity switching can be induced by a sequence of pulses of varying pulse width at a fixed voltage amplitude.

Nagao et al. [28] has reported the transmission electron microscopy (TEM) and selected area electron diffraction (SAED) studies on the BSMO system and found that the structural modulations of the system consist of transverse modulation associated with the Pcnn-type symmetry. Gupta et al. [29] reported room temperature real space atomically resolved scanning tunneling microscope (STM) studies of $Bi_xSr_{1-x}MnO_3$ ($0.25 \le x \le 0.75$) samples. The images show the presence of CO phase consisting of charge-ordered phase coexisting with charge-disordered (CD) phase. The high temperature specific heat measurements have provided the $T_{CO}(x)$ phase diagram of the system.

In recent years the properties of manganites have been analyzed in view of the concept of electronic phase separation (PS). The natural tendency of phase separation in manganites is explained by Castello et al. [30] from the X-ray absorption fine structure (EXAFS) at the Mn K-edge and dc magnetic measurements on Cu doped La-manganites. Joshi et al. [31] used Griffiths phase physics to explain temperature dependent electrical resistivity, AC susceptibility and electron spin resonance (ESR) data on $La_{0.67}Ca_{0.33}Mn_{0.93}Fe_{0.07}O_3$. PS model is used by Cortés-Gil et al. [32] to explain the magnetization data on $La_{1-x}Ca_xMnO_3$ ($0 < x < 1$) and $La_{1-x}Sr_xMnO_3$ ($x < 0.6$). The evolution of the magnetic response of the system was understood by identifying the signatures of the nucleation of AFM and FM phases. It is found that the size of the FM clusters increase with the increase in tolerance factor. The electrical and magnetic studies on $Y_{0.4}Ca_{0.6}MnO_3$ by Ling et al. [33] showed the evolution of FM clusters in the bulk AFM–CO state with decreasing temperature. Magnetocaloric measurements on $La_{5/8-y}Pr_yCa_{3/8}MnO_3$ and $Pr_{0.5}Ca_{0.09}Sr_{0.41}MnO_3$ by Quintero et al. [34], showed an adiabatic temperature change during a metamagnetic transition from AFM to FM phase. The competition between coexisting AFM and FM phases resulted in the low temperature state of both the systems. The phase-separation concept was used by Mohan et al. [35] to explain the resistivity data on $Sm_{0.55}Sr_{0.45}MnO_3$. From the transport and magnetic studies on $R_{1-x}Ca_xMnO_3$ (R, a rare-earth element, $x = 0.88$–1). Wang et al. [36] concluded that FM clusters are embedded in an AFM matrix of these mix-valent manganites at low temperatures. A percolative type conduction transport between the FM clusters takes place in the phase separated state. The CMR effect observed in the phase separated state is considered to be due to contributions from rotation of the FM domains.

A number of studies on Bi-based manganites have also reported the coexistence of FM and AFM phases. The temperature and magnetic field dependent small angle neutron scattering (SANS) measurements on $Bi_{0.125}Ca_{0.875}MnO_3$ by Qin et al. [37] revealed the formation of FM spin clusters in an AFM background when temperature was decreased to ~108 K. Lowering the temperature further or the application of external magnetic field increased the number of clusters resulting in an overall enhancement of magnetization below T_C. In $Bi_{0.5}Sr_{0.5}Fe_xMn_{(1-x)}O_3$ compounds the magnetic state changes from paramagnetic (PM) to weak AFM as temperature is decreased [38]. The thermomagnetic behavior is related to the coexistence of AFM and FM fluctuations in the PM state. In AFM state, zero field cooled/field cooled (ZFC/FC) thermomagnetic hysteresis is attributed to the formation of small FM clusters. The studies on $Bi_{0.8}Ca_{0.2}FeO_3$ with Mn-substitution at Fe-site, showed the samples to be in AFM state with small FM clusters [39]. Magnetic and transport studies on $Bi_{0.1}La_{0.5}Ca_{0.4}MnO_3$ [40] showed the existence of CO, weak and strong FM and a blocked metastable state with decrease in temperature. The CO and FM phases coexist at low temperatures. The ESR studies on $La_{(0.5-x)}Bi_xCa_{0.5}MnO_3$ by Li et al. [41] showed the enhancement of T_{CO} with increasing Bi content and the coexistence of FM and AFM domains in the PM matrix.

In our earlier studies we reported detailed temperature dependent ESR and resistivity measurements on bulk samples of $Bi_{(1-x)}Ca_xMnO_3$ [42,43], Cr-doped $Bi_{0.5}Ca_{0.5}MnO_3$ [45] and $Bi_{0.6}Ca_{(0.4-x)}Sr_xMnO_3$ [46] compounds. We also reported the temperature dependent ESR studies on nanoparticles of $Bi_{0.55}Ca_{0.45}MnO_3$ [44]. The data in these studies were analyzed in view of phase separation (PS) model. The evolution and competition between the FM and AFM phases as a function of composition and temperature is highlighted in these studies. In this paper we report the temperature dependent ESR and resistivity studies of charge ordered $Bi_{(1-x)}Sr_xMnO_3$ ($x = 0.3$, 0.4, 0.45, and 0.5). Our data show a strong competition between AFM and FM phases as a function of composition and temperature.

2. Experimental details

The bulk samples of $Bi_{(1-x)}Sr_xMnO_3$ ($x = 0.3$, 0.4, 0.45, and 0.5) were synthesized by conventional solid state reaction method. The appropriate amounts of Bi_2O_3, $SrCO_3$, and MnO_2 were ground and mixed using the agate mortar. The compound was then sintered at temperatures ranging from 800 °C to 950 °C for about 30 h with intermediate grinding. The samples were checked for single phase formation from the XRD patterns recorded on PHILIPS X-ray diffractometer with a Cu X-ray source. The ESR spectra of the samples were recorded on powder samples using a Joel X-Band ESR spectrometer in the temperature range 125–475 K. The pellets of

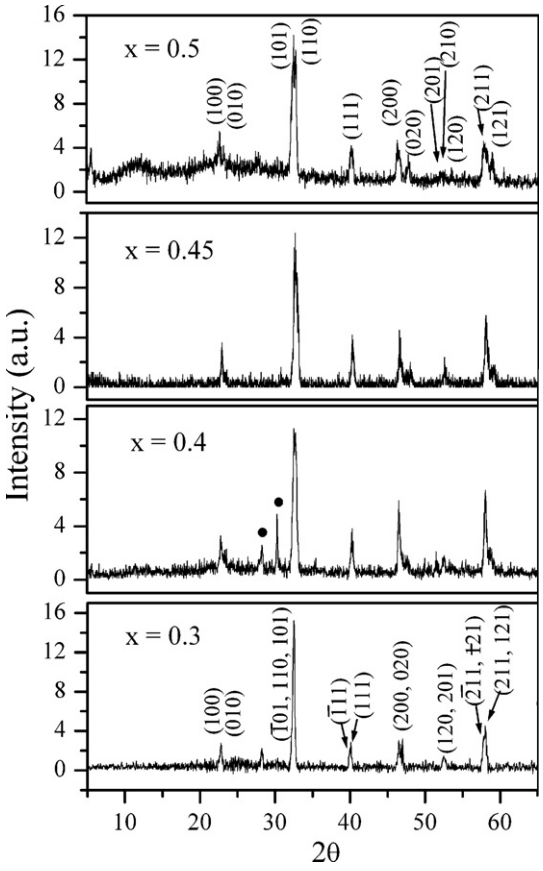

Fig. 1. XRD plots for various compositions of $Bi_{(1-x)}Sr_xMnO_3$ system.

the synthesized powder material were made and sintered at 900 °C for 12 h. The resistivity measurements were made on rectangular shaped samples cut from the sintered pellets by four-probe method using a closed cycle refrigerator (CCR) fitted with a Lakeshore 330 temperature controller.

3. Results and discussion

3.1. X-ray diffraction (XRD) results

The objective of the XRD studies is to assess the single phase formation of the synthesized material. Fig. 1 shows the XRD plots of the $Bi_{(1-x)}Sr_xMnO_3$ (x = 0.3, 0.4, 0.45, and 0.5) samples. The earlier reports have established that the structure of the BSMO changes from monoclinic to tetragonal as x increases from 0.3 to 0.5 [47]. The peaks in the XRD plots were indexed in view of the perovskite structure. The lattice parameters for a perovskite structure are given as $a = c \approx b \approx a_p$, where a_p is the lattice parameter of the cubic perovskite structure. A rough estimate of the structure and lattice parameters of the present samples was made. The XRD data was analyzed for tetragonal structure (~orthorhombic) and the lattice parameters obtained are $a \approx c \neq b$ for x = 0.5 sample. The double peak in the XRD plot characteristic of the tetragonal structure and observed at $2\theta = 33^\circ$ of x = 0.5 sample was not observed of x = 0.3 sample. This manifests the beginning of the change in the structure from a symmetrical to an asymmetrical one. The samples undergo a first order transition of the crystal structure which can be attributed to the difference in the ionic radii Mn^{3+} (0.645 Å)/Mn^{4+} (0.53 Å) ratio. The impurity peaks observed (marked with black dots above the peak in the x = 0.4 sample) could be due to the unreacted Bi_2O_3, MnO_2 or due to the formation of Bi_2SrO_4 phase [48]. The estimated lattice parameters are $a \approx c \approx 3.92$ Å and $b \approx 3.88$ Å for x = 0.3 sample (~monoclinic structure) and $a \approx c \approx 3.9$ Å and $b \approx 3.78$ Å for x = 0.5 samples (~tetragonal structure), similar to that reported in reference [47].

3.2. ESR studies

The ESR is a sensitive probe of the local magnetization of PM, FM and AFM regions relying on the distinct difference in the corresponding resonance spectra. ESR is also particularly sensitive to sample inhomogeneities. It is known that manganites are ESR active showing a temperature dependent variation in the double integrated resonance line intensity (DI) and linewidth (ΔH). The most common Mn ion that can contribute to an ESR signal is Mn^{2+} (S = 5/2). As Mn^{3+} (S = 2) ions show a large zero field splitting and strong spin lattice relaxation it is thought unlikely to exhibit an observable ESR signal [49]. Mn^{4+} ions are known to contribute to ESR signal due to the weak spin-lattice relaxation. It has been pointed out that in manganites the ESR signal is observed due to all Mn ions in the form of some combination or clusters of Mn^{3+}–Mn^{4+} ions coupled by strong short-range FM double-exchange (DE) interactions [49,50].

Fig. 2 shows the ESR spectra for x = 0.5 and x = 0.3 samples in the temperature range 120–450 K. Similar spectra were observed for other compositions. The ESR signal for the half doped sample is symmetric at all temperatures. While for the Bi-rich sample it is slightly asymmetric in the entire temperature range. On cooling from high temperature the intensity of the spectra shows a little change for x = 0.5 sample and it increases for x = 0.3, 0.4 and 0.45 samples until the temperature of ~200 K followed by a rapid decrease with further decrease in temperature indicating the onset of the long range AFM ordering in the sample. A small kink in the spectra is observed at ~300 mT for x = 0.3 sample (shown circled in Fig. 2). The intensity of this signal is dependent on the material processing. This signal is not observed for well processed samples, e.g. for x = 0.5 sample (Fig. 2). This feature may be due to the existence of the FM cluster inhomogeneities in the sample. The DI of this signal is temperature independent. The temperature dependence of DI of the main ESR signal is not affected by the presence of this kink in the ESR spectra and hence the conclusions drawn in the present study are not affected. The g value estimated for all the compositions is ~2 and remains almost temperature independent throughout the temperature range. The spectra can be fitted to a Lorentzian line shape, for the entire temperature range. This confirms that the size of the sample is smaller than the skin depth of the penetrating microwaves used. Hence any change seen in the signal intensity or peak linewidth is purely an intrinsic property of the sample and not due to skin depth effect.

Fig. 3 shows the temperature dependent DI of the ESR spectra for various samples. In our earlier work we identified the T_{CO} and T_N from the DI vs temperature (T) plots for the $Bi_{(1-x)}Ca_xMnO_3$ system [42,43]. For comparison purpose we have taken DI vs T plot for $Bi_{0.5}Ca_{0.5}MnO_3$ (BCMO) from Refs. [42,43] and used it as a reference to identify the features characteristic of T_{CO} and AFM onset temperature, T_O. The absence of high temperature peak characteristic of CO in these plots confirms that charge ordering is above ~470 K (maximum temperature possible in our experimental setup) in these samples. The temperature below which DI decreases rapidly is depicted as T_O. The values of T_{CO} reported in the literature are listed in Table 1. The data for BSMO samples are in the temperature range, $T < T_{CO}$.

The validity of Curie–Weiss law at higher temperatures for BSMO has been addressed in earlier studies [21,42,43,51,52]. Since the present data are at temperatures below T_{CO}, the validity of the Curie–Weiss law is explored in the CO state of the samples. A linear fit is obtained until T_O for the x = 0.3 sample (Fig. 4). The positive value of the intercept on the temperature axis indicates the presence of FM correlations. When T_O is approached the FM correlations

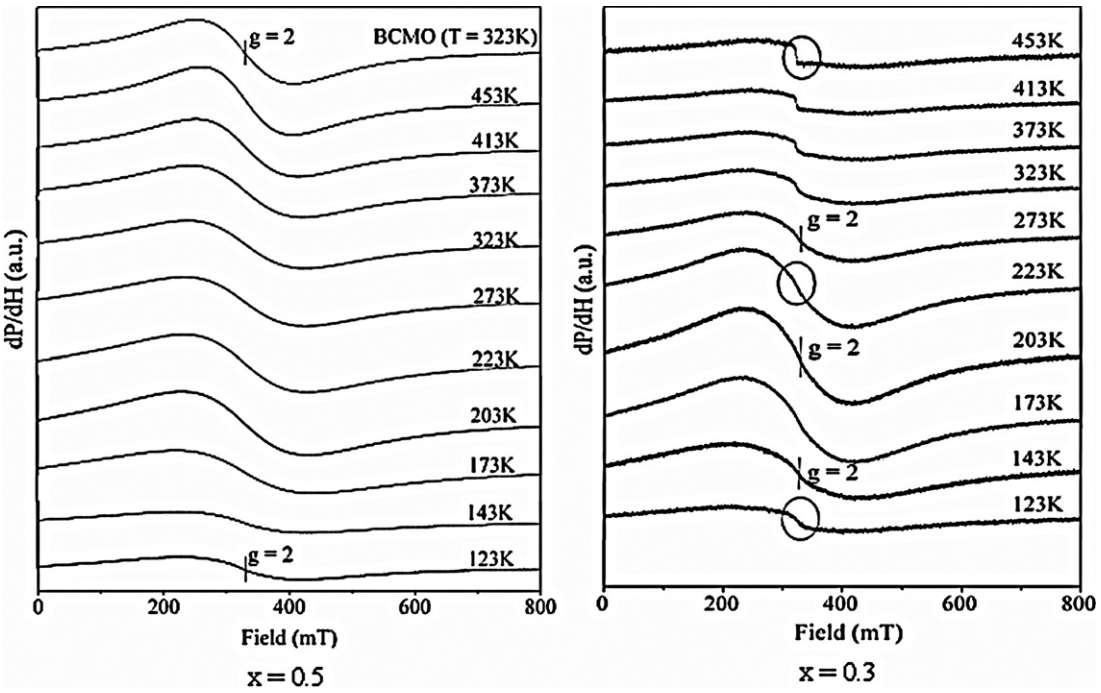

Fig. 2. Representative temperature dependent ESR spectra for $Bi_{(1-x)}Sr_xMnO_3$ sample with $x = 0.5$ and $x = 0.3$. For comparison the ESR spectra for $Bi_{0.5}Ca_{0.5}MnO_3$ (BCMO) at 323 K from Refs. [42,43] is also shown.

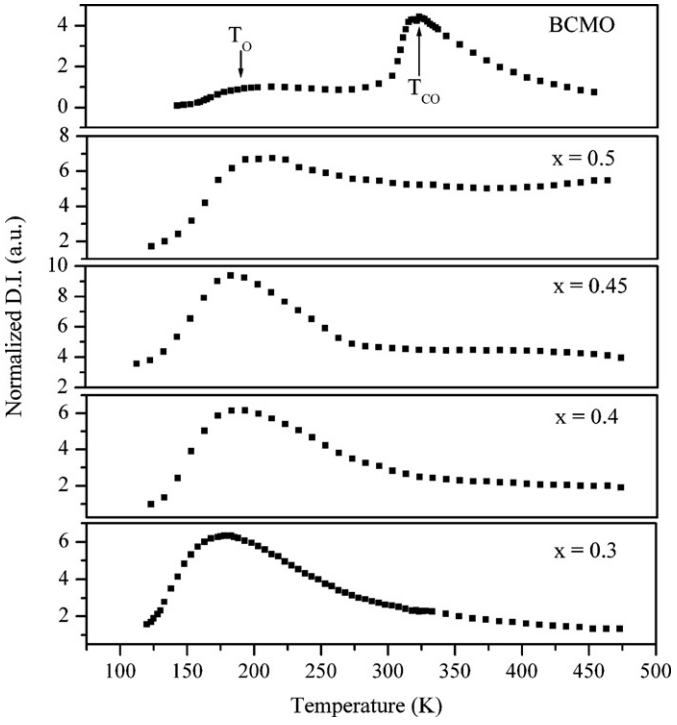

Fig. 3. DI vs T plots for the $Bi_{(1-x)}Sr_xMnO_3$ system and the reference data for $Bi_{0.5}Ca_{0.5}MnO_3$ (BCMO) sample taken from Refs. [42,43].

Table 1
The T_N values obtained from the ΔH vs T and the resistivity plots and the T_{CO} values from Refs. [24,42,43].

Sample x	$T_{N(ESR)}$ (K)	$T_{N(res)}$ (K)	T_{CO} (K)
0.3	133	151	600
0.4	153	133	575
0.45	163	122	540
0.5	173	105	525
BCMO	160	95	317

diminish leading to deviation from the linear fit. The data for sample with $x = 0.4$ can be fitted to two straight lines of different slopes. The change of slope occurs at ~320 K. The slope of the straight line fit in the 320–475 K temperature range gives a negative intercept on the temperature axis. This indicates the enhanced AFM correlations below T_{CO}. In the temperature range ~320 K–T_O, the linear fit gives a positive intercept indicating strengthening of FM correlations with

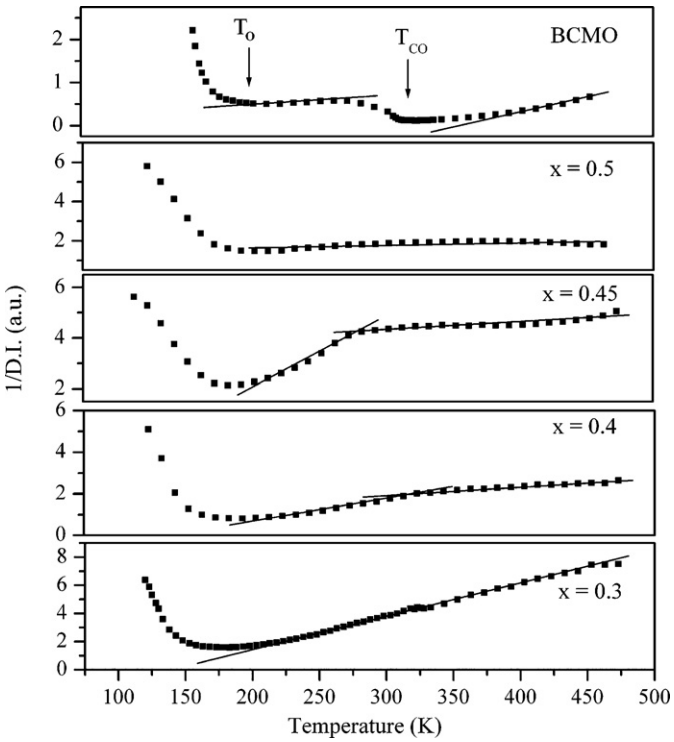

Fig. 4. 1/DI (χ_{ESR}) vs T plots for the $Bi_{(1-x)}Sr_xMnO_3$ system and the reference data for BCMO sample taken from Refs.[42,43].

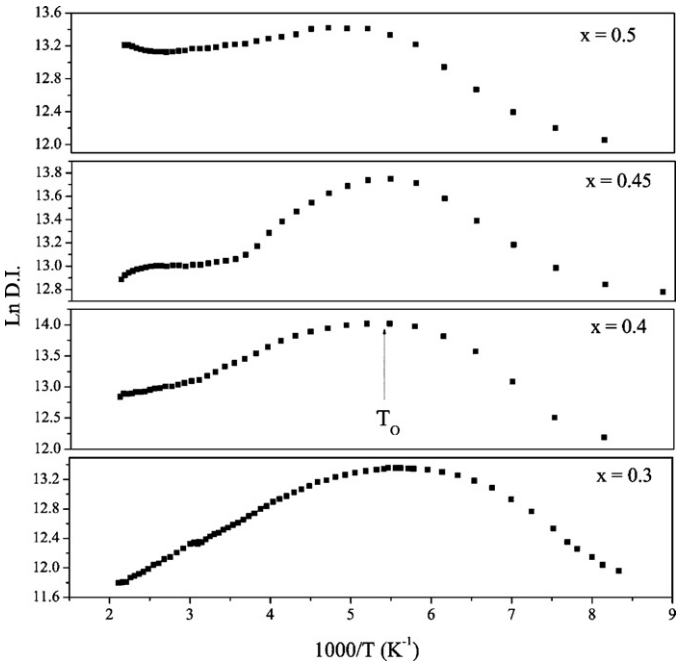

Fig. 5. ln DI (χ_{ESR}) versus 1000/T plots for the $Bi_{(1-x)}Sr_xMnO_3$ system.

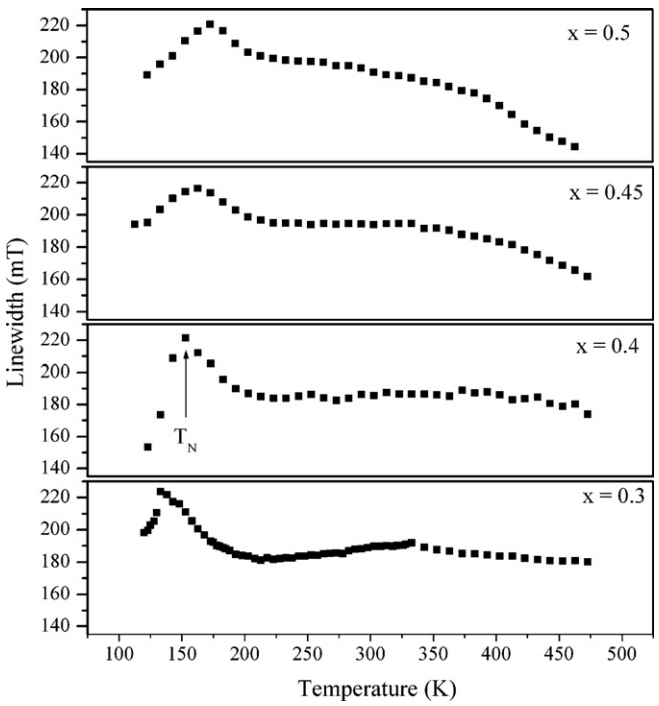

Fig. 6. Temperature dependent linewidth of the BSMO system.

decrease in temperature. A similar situation is found for $x = 0.45$ sample. Two straight line fits for 1/DI vs T plots, one for $T > 275$ K with negative intercept on T-axis and the other for $T < 275$ K with positive intercept on the T-axis are obtained. For the sample with $x = 0.5$, only one linear fit with a negative intercept on the T-axis is obtained. This indicates the domination of AFM correlations in the CO state of this composition.

Fig. 5 shows ln DI vs 1000/T plots for the present system. Such plots are useful to get information about magnetic interactions [53,54]. The domains of FM and AFM spin correlations coexist in the temperature range $T > T_N$. The contribution of AFM correlations progressively increase with the increase in Sr content as indicated by the decrease in slope of ln DI vs 1/T plot in the temperature range $T_O < T < 475$ K. For the sample with $x = 0.5$, the weak temperature dependence of ln DI on T indicates the balance between FM and AFM spin correlations. The sudden decrease in ln DI at low temperatures indicates the onset of long range AFM ordering. But the FM correlations exist even below ~125 K. This is evident from the narrow ESR spectra observed below T_N.

The samples are in the CO phase in the temperature range used for ESR studies. These studies show that with decreasing temperature the contribution from FM spin correlations decrease and the AFM spin correlations emerge i.e. the domains of FM and AFM spin correlations coexist in this temperature range. These studies strongly suggest the existence of two-phase behavior in the temperature range $T > T_N$. The phase separation between FM and AFM domains in the CO state has been predicted to be universal for manganites [55].

Fig. 6 shows the variation of ΔH with temperature for various samples. In the CO state, ΔH first increases, remains constant over a temperature range and then increases again with decrease in temperature for samples with $x = 0.45$ and 0.5. Whereas ΔH remains constant with decrease in temperature for the samples with $x = 0.4$ and 0.3. For all samples ΔH reaches a peak value at Neel temperature, T_N, followed by a sharp decrease with further decrease in temperature. The ΔH variation exhibited by $x = 0.5$ sample is similar to that seen for BCMO system in the temperature range $T < T_{CO}$ [56]. The initial increase in the ΔH value with decrease in temperature suggests that the T_{CO} for this sample is lower than that of $x = 0.4$ and 0.3 samples. These results show that increase in substitution of a divalent ion at Bi site gives rise to changes in the temperature dependence of DI and ΔH which can be related to changes in the volume fraction of FM and AFM domains in the system.

The initial increase in the ΔH values with decreasing temperature for samples with $x = 0.45$ and 0.5 indicates that T_{CO} is in the vicinity of ~500 K as reported in the literature [24]. The absence of initial increase in ΔH value in the case of $x = 0.3$ and 0.4 samples clearly suggests the higher T_{CO} values for these samples. The T_N values for various samples are given in Table 1. In the BSMO system effective A-site cationic radius increases with increase in Sr content leading to decrease in T_{CO}. Whereas for BCMO system effective A-site cationic radius decreases with increase in Ca content leading to decrease in T_{CO}. The different trends in T_{CO} variation for these systems are due to the difference in the effective ionic radius of the Bi^{3+} and its orbital character. The effective A-site ionic radius is 1.24 Å with a dominant $6s^2$ character when Sr^{2+} is substituted at Bi^{3+} site. Whereas it is 1.16 Å with a constrained $6s^2$ character when Ca^{2+} is substituted at Bi^{3+} site [17,57].

The concept of phase separation has been used to analyze the ESR data on other manganites also viz. $La_{1-x}Pb_xMnO_3$ and $Nd_{0.5}Sr_{0.5}MnO_3$ [58,59].

3.3. Resistivity studies

The temperature dependent resistivity data of $Bi_{(1-x)}Sr_xMnO_3$ are shown in Fig. 7. The plots show a strong semiconducting behavior with values of resistivity (ρ) reaching $\approx 10^7$ Ω cm at 80 K. The data below this temperature could not be recorded as the resistance of the sample was too high to measure. At a certain temperature there is a sudden increase in the resistivity with decreasing temperature (inset of Fig. 7). This is the Neel temperature, T_N, at which the long range AFM ordering takes place in the sample. The T_N values for various samples are listed in Table 1. It has been pointed out in Refs. [60,61] that this type of resistivity behavior is typical of manganites with CO and OO. The increase in Sr content decreases the resistivity due to the increased amount of hole doping, which is in agreement with the previously reported work [42,43]. The Bi^{3+}

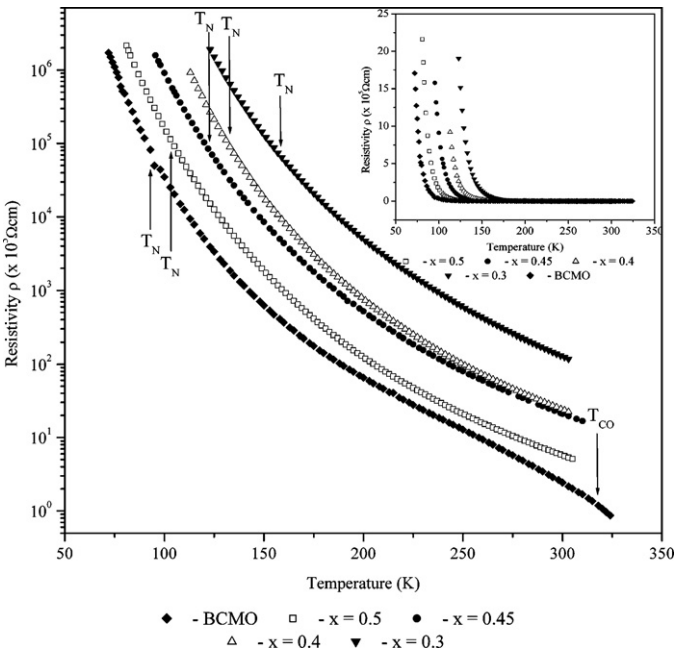

Fig. 7. The resistivity vs temperature plots of the $Bi_{(1-x)}Sr_xMnO_3$ and the BCMO systems.

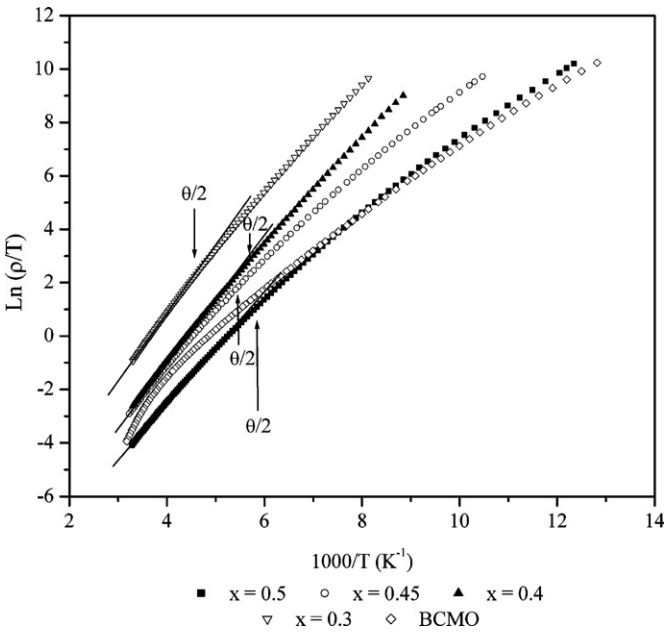

Fig. 8. $\ln(\rho/T)$ vs $1000/T$ plot for the BSMO and the BCMO system.

ion has a highly polarizable $6s^2$ lone pair of electrons which can have a marked effect on the properties exhibited by the BSMO system. More dominant the $6s^2$ lone pair character, bigger will be the effective size of Bi^{3+} ion, which presumably distorts the oxygen coordination. The earlier works by Garcia-Munoz et al. [17] and Frontera et al. [57] suggest the electron density of the $6s^2$ lone pair to be high along some Bi–O bonds. This in turn renders the electronic density to be involved in strong covalent interactions with Bi–O bonds producing an effective bigger Bi^{3+} ion. As the Sr content increases $6s^2$ lone pair effect decreases due to the decrease in Bi^{3+} content.

The e_g bandwidth decreases as the effective size of the A-site cation decreases. This favours charge localization and hence increase in resistivity [17,57]. An estimation of average A-site cationic radius, $\langle r_A \rangle$, proves that it decreases with decrease in the Sr content. The characteristic feature of CO transition is not observed in the resistivity data, indicating that T_{CO} for BSMO system is beyond the measurement temperature range of the experiment. It is noted that the T_N values estimated from ESR and resistivity data are different. This is because ESR being an atomic probe is more sensitive to small changes in the magnetic correlations at atomic level. Whereas resistivity being a bulk property, registers changes only when the bulk of the sample contributes to the resulting change.

The resistivity data are analyzed in view of two different approaches (1) small polaron model and (2) variable range hopping (VRH) model. The small polaron model has been widely used to analyze the transport properties of La-manganites [62,63]. According to this model electrical conduction in the high temperature regime $T > \theta_D/2$, where θ_D is the Debye temperature, takes place by thermal activation of the charge carriers and the resistivity is given by

$$\rho = \rho_0 T^n \exp\left(\frac{W}{k_B T}\right) \quad (1)$$

where $n = 1$ and 1.5 for adiabatic and non-adiabatic conduction mechanism, respectively, W is activation energy and k_B is Boltzmann's constant [64–70].

Fig. 8 shows the $\ln(\rho/T)$ vs $1000/T$ plots as per Eq. (1) with the value of $n = 1$ (adiabatic hopping). The plots show a linear variation of $\ln(\rho/T)$ in the high temperature range. The deviation from linearity starts at a temperature which can be taken as $\theta_D/2$ as per the polaron model. Similar plots are obtained for $n = 1.5$. The activation energy values are calculated for both the cases and given in Table 2. The activation energy of hopping conduction for $T > \theta_D/2$ can be written as [66].

$$W = W_H + \frac{W_D}{2} \quad (2)$$

where W_H and W_D are hopping and disorder energy, respectively.

In the polaron model W_H decreases with the decrease in temperature. For a temperature $T < \theta_D/4$, $W \approx W_D$. Since the resistivity of the sample at low temperatures is very high, the measurement in the temperature range below $\theta_D/4$ was possible only for sample with $x = 0.5$. The estimated W_D for this sample is ~0.01 eV which is close to the theoretically predicted value as per the polaron model.

The polaron model can be used to explain the conduction mechanism in the BSMO system in the high temperature regime. The strong insulating behaviour coupled with high room temperature resistivity is indicative of strong localization of the itinerant electron, i.e. strong Anderson localization in the system [71–75]. It is not possible from $\ln(\rho/T)$ vs $1/T$ plots to ascertain whether the hopping is adiabatic ($n = 1$) or non adiabatic ($n = 1.5$). A plot of $\log_{10}\rho$ vs W can resolve this issue [76]. If the T value estimated from the slope of the plot is close to the temperature at which the $\log_{10}\rho$ value is taken, then the polaron hopping is in the adiabatic regime. If it is very different, then it is in the non-adiabatic regime. Fig. 9 shows $\log_{10}\rho$ vs W plots for the BSMO system at 300 K. The estimated $T \approx 354$ K obtained from the slope $1/k_B T$. This value being close to 300 K (temperature at which the value of resistivity is taken) confirms the polaron hopping conduction to be in the adi-

Table 2
Debye temperature and activation energies from the thermally activated polaron hopping model for $n = 1$ and 1.5 for the $Bi_{(1-x)}Sr_xMnO_3$ system.

Sample x	ρ (Ω cm)	θ (K)	W for $n = 1$ (meV)	W for $n = 1.5$ (meV)
0.3	125	430	226	226
0.4	23.5	394	211	211
0.45	21	390	198	198
0.5	5.6	375	178	189

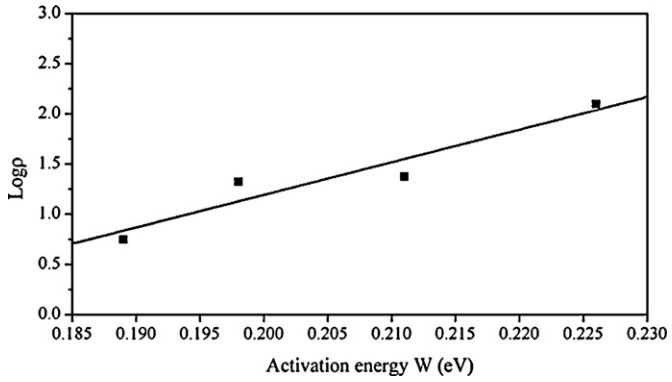

Fig. 9. Log_{10}(resistivity) vs activation energy, W.

abatic regime. This means that the resistivity is dependent on the activation energy alone and the pre-exponential factor in Eq. (1) does not play any significant role.

The resistivity data are also analyzed using Mott's VRH model which considers an energy independent density of states and Efros–Shklovskii VRH (ES-VRH) model which takes into consideration the long range electron–electron Coulomb interaction, which in turn forms a Coulomb gap (CG). The general equation of the VRH model is given as

$$\rho(T) = \rho_0 \exp\left(\frac{T_0}{T}\right)^P \tag{3}$$

where p is the hopping exponent and T_0 is the characteristic temperature. Generally, the value of p depends on the mode of hopping of charge carriers at low temperatures [77,78]. The Mott's VRH model assumes a small p value like 1/3 or 1/4 for a two-dimensional or three-dimensional systems, respectively, while for a scenario where the density of states is strongly energy dependent, like in the ES-VRH model, p takes a larger value of 1/2.

The resistivity data are analyzed using Motts VRH model [69,70] equation

$$\rho = \rho_0 \exp\left\{2.06\left[\frac{\alpha^3}{N(E_F)kT}\right]^{1/4}\right\} \tag{4}$$

with

$$kT_0 = \frac{18\alpha^3}{N(E_F)} \tag{5}$$

where $N(E_F)$ is the density of states at the Fermi level and α is the inverse of the localization length $\xi \sim 1/\alpha$. The density of states near the Fermi level is assumed to be constant in the derivation of the above equation. In the VRH model the average hopping distance and hopping energy at room temperature T, are given by

$$R^4 = \frac{9}{8\pi\alpha k_B T N(E_F)} \tag{6}$$

and

$$W = \frac{3}{4\pi R^3 N(E_F)} \tag{7}$$

respectively with the energy difference between the initial and final states over which the electrons hop given by [79]

$$\delta_M = \frac{1}{4}k_B T\left(\frac{T_0}{T}\right)^{1/4} \tag{8}$$

Fig. 10 shows $\ln\rho$ vs $1/T^{(1/4)}$ plots for various samples. Two straight lines can be fit to these plots. The temperatures at which these lines intersect are same as the T_N values obtained from the ESR data. The T_0 values of Eq. (5) estimated from the slope of these

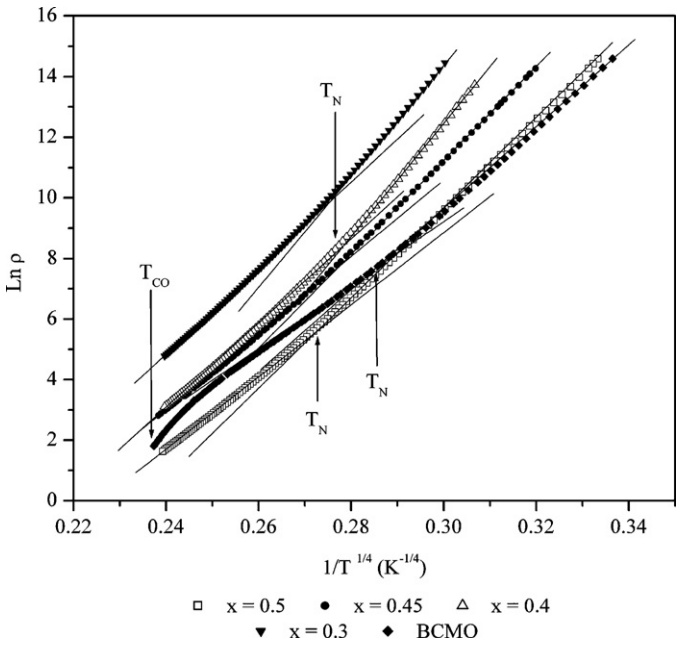

Fig. 10. Ln ρ vs $1/T^{(1/4)}$ plots of the $Bi_{(1-x)}Sr_xMnO_3$ and the BCMO systems.

Table 3
The T_0 and ρ_0 values obtained from ln ρ vs $T^{-1/4}$ plots in different temperature ranges for the $Bi_{(1-x)}Sr_xMnO_3$ system.

Sample x	T_0 (10^8 K)		ρ_0 (Ω cm)	
	$T_{CO} > T > T_N$	$T < T_N$	$T_{CO} > T > T_N$ ($\times 10^{-13}$)	$T < T_N$ ($\times 10^{-19}$)
0.3	3.9	10.6	2.9	57.5
0.4	3.0	12.3	4.5	1
0.45	2.2	5.5	41.4	9320
0.5	2.0	4.9	20.9	6840

plots are listed in Table 3. The increase in T_0 in the AFM state can be due to decrease in $N(E_F)$ and/or ξ.

The studies on La-based manganites suggested that it was either the density of states or the localization mechanism which played an important role in determining the resistivity behaviour [80]. It has been proposed that a random potential of mainly magnetic origin is responsible for carrier localization above T_C. With decreasing temperature the AFM interactions continuously increase and may enhance the localization and reduce the density of states. The localization length must be greater than Mn–Mn distance which is ~5 nm, and the hopping distance should be several times that of Mn–Mn distance. Keeping this in mind the values of localization length, hopping distance and hopping energy are estimated adopting a reasonable value of $N(E_F) \sim 10^{21}$ cm^{-3} eV^{-1} [81]. The hopping distance is found to be several times the Mn–Mn distance and the localization length greater than the Mn–Mn distance. The estimated values are given in Table 4. These values present a

Table 4
Various Mott VRH model parameters estimated for $Bi_{(1-x)}Sr_xMnO_3$ using $N(E_F) \approx 3 \times 10^{21}$ cm^{-3} eV^{-1} in different temperature ranges.

Sample x	ξ (Å)		R (nm)		W (meV)	
	$T_{CO} > T > T_N$	$T < T_N$	$T_{CO} > T > T_N$	$T < T_N$	$T_{CO} > T > T_N$	$T < T_N$
0.3	8.2	5.8	10.3	9.5	218	280
0.4	8.9	5.5	10.5	9.4	205	291
0.45	6.8	5.0	7.5	6.9	189	238
0.5	7.0	5.2	7.6	7.0	185	231

physically acceptable situation. The ESR studies indicate that the dominant FM interactions at higher temperatures weaken with the decrease in temperature because of the progressive growth of AFM interactions, which in turn may lead to localization of carriers and reduction of $N(E_F)$.

The resistivity data are also analyzed using the VRH model developed by Efros and Shklovskii, i.e. (ES-VRH) model which takes into account the electron–electron Coulomb interaction [82,83]. There are reports of this model being used to explain the conduction mechanism for manganites [84]. It was suggested that the Coulomb interaction may have an important effect on the hopping conduction of electrons in manganese oxides [85,86] and other oxide semiconductors [87,88]. According to the Efros–Shklovskii interaction theory the density of localized states is diminished in the immediate neighbourhood of the Fermi level due to Coulomb interaction and the minimum resultant is called Coulomb Gap (CG). The resistivity at low temperatures due to the existence of the CG follows the expression

$$\rho = \rho_0 \exp\left(\frac{T_0}{T}\right)^{1/2} \tag{9}$$

where T_0 is the characteristic temperature and ρ_0 is the ES residual resistivity. The value of T_0 is estimated from $\ln\rho$ vs $T^{-1/2}$ plot. The localization length ξ is given by the equation

$$\xi = \frac{\beta_1 e^2}{4\pi\varepsilon_0\varepsilon_r k_B T_0} \tag{10}$$

where e is the electronic charge, k_B is the Boltzmann constant, ε_0 is the permitivitty of free space and ε_r is the dielectric constant. There exists a discrepancy regarding the value of β_1, which depends on the space dimensionality. According to Efros–Shklovskii [89,90] and Matthias Mayr et al. [91] β_1 takes a value of 2.8, while Adkins [92] reported a value of 0.57. The value predicted by Efros–Shklovskii has been reported for a variety of materials [79,93,94]. The value of the dielectric constant for the BSMO system has been reported as $\sim 10^6$ for a wide range of frequencies [81]. The values of T_0 and ξ are used to estimate the hopping distance, R_{ES}, and the hopping energy, E_{ES}, using the equations

$$R_{ES}(T) = \frac{1}{4}\xi\left(\frac{T_0}{T}\right)^{1/2} \tag{11}$$

and

$$E_{ES}(T) = \frac{1}{2}K_B T\left(\frac{T_0}{T}\right)^{1/2} \tag{12}$$

respectively, with the energy difference between the initial and final states over which the electrons hop is given by the equation [79]

$$\delta_E = \frac{1}{4}K_B T\left(\frac{T_0}{T}\right)^{1/2} \tag{13}$$

Further, the necessary criteria to be satisfied for the conduction to occur in the VRH model [57] are (i) the average hopping energy, $E_{ES} > k_B T$ and (ii) $\xi R_{ES} > 1$.

Fig. 11 shows $\ln\rho$ vs $T^{-1/2}$ plots for various samples. A linear fit in the entire temperature range, i.e. below T_{CO} is obtained for $x = 0.45$ and 0.5 samples. For samples with high resistivity there is a change of slope at T_N. The conditions (i) and (ii) are satisfied for all the samples throughout the temperature range as shown in Table 5. However, the estimated $\xi \approx 10^{-6}$ Å is not of the order of unit cell dimension and hence unreasonable (Table 6). This may be due to fact that the energy scale of fitting region ($T \leq 300$ K) is very high in comparison with the ordinary size of the Coulomb gap (10–100 K) [83,95]. In view of this it is unlikely that the observed ES-type behaviour is due to the emergence of the Coulomb gap. The Mott insulating ground state in the BSMO system is confirmed

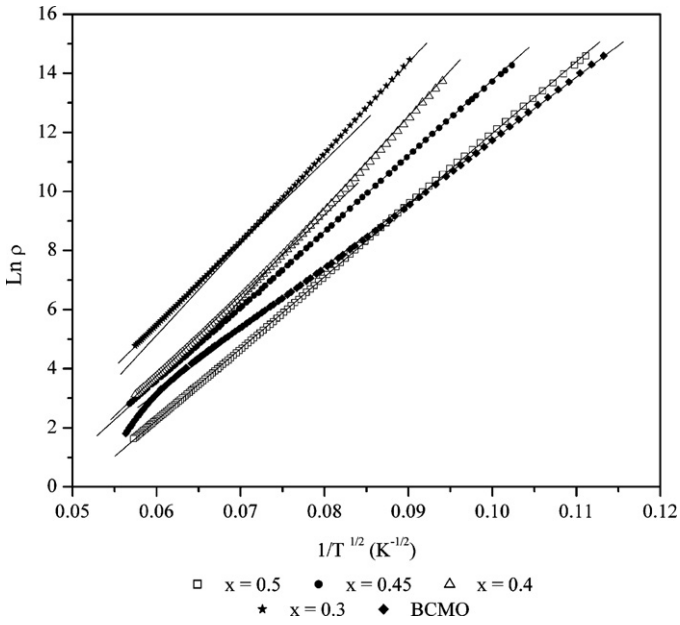

Fig. 11. $\ln\rho$ vs $1/T^{(1/2)}$ plots of the $Bi_{(1-x)}Sr_xMnO_3$ and the BCMO systems.

Table 5
The T_0 and ρ_0 values obtained from $\ln\rho$ vs $T^{-1/2}$ plots in different temperature ranges for the $Bi_{(1-x)}Sr_xMnO_3$ system.

Sample x	T_0 (10^4 K)		ρ_0 ($\times 10^{-6}$ Ω cm)	
	$T_{CO} > T > T_N$	$T < T_N$	$T_{CO} > T > T_N$	$T < T_N$
0.3	7.92	9.25	11.2	2.22
0.4	7.29	9.497	3.93	0.23
0.45	6.44	6.44	8.61	8.61
0.5	5.895	5.895	4.51	4.51

from the fact that the AFM ordering takes place in the insulating phase. There is coexistence of clusters of competing phases as a result of phase separation in the BSMO system. It is quite likely that the magnetic phase separation (PS) or inhomogeneities may be responsible for resistivity behaviour similar to that predicted by ES-VRH model.

The present resistivity data can be qualitatively analyzed in view of the percolation model for mixed phase manganites [91]. Samples with dominant AFM interactions (domains) which grow at the expense of the FM domains can give rise to increase in resistivity, which will be evident even at room temperature. With decrease in temperature the AFM (insulating) domains grow progressively at the expense of FM (metallic) domains giving rise to increase in resistivity. The FM cluster size decreases as the long range AFM order sets in. The volume fraction occupied by FM clusters is very small compared with the volume of the AFM phase. The sharp increase in resistivity observed below T_N, therefore, may be due to quite low connectivity between FM clusters.

Table 6
Various ES VRH model parameters estimated for $Bi_{(1-x)}Sr_xMnO_3$.

Sample x	ξ ($\times 10^{-6}$ Å)		R ($\times 10^{-5}$ Å)		E (meV)	
	$T_{CO} > T > T_N$	$T < T_N$	$T_{CO} > T > T_N$	$T < T_N$	$T_{CO} > T > T_N$	$T < T_N$
0.3	5.9	5.1	2.4	2.22	210	227
0.4	6.4	4.9	2.5	2.19	202	230
0.45	7.26	7.26	2.66	2.66	189	189
0.5	7.94	7.94	2.78	2.78	182	182

4. Conclusions

In conclusion, we report the temperature dependent electron spin resonance (ESR) and electrical resistivity studies of $Bi_{(1-x)}Sr_xMnO_3$ ($x = 0.3$, 0.4, 0.45, and 0.5). The double integrated (DI) intensity of the ESR signal vs temperature and ln DI vs $1000/T$ plots have been used to get information about magnetic interactions. A sharp change in the slope of ln DI vs $1000/T$ plot indicates the onset of long range AFM order. The Neel temperature (T_N) of the sample is found to increase with increase in Sr content. In the temperature range $T > T_N$ domains of ferromagnetic (FM) and antiferromagnetic (AFM) correlations co-exist. The contributions of AFM correlations increase with the increase in Sr content. The observation of weak ESR signal in the temperature range below T_N indicates the freezing of FM microdomains/inhomogeneities in the AFM long range ordered state.

The temperature dependent resistivity data are analyzed in view of polaron model. It is observed that the conduction takes place by small polaron hopping in the adiabatic regime in the temperature range $T > 200$ K. The resistivity data are analyzed in view of both Mott's VRH model as well as ES-VRH model. It is seen that $\ln \rho$ varies linearly with $T^{-1/4}$ with a change in slope at $T = T_N$. The density of states $\sim 10^{21}$ cm^{-3} eV^{-1} gives physically acceptable values of average hopping distance and the localization length. Although the linear variation of $\ln \rho$ with $T^{-1/2}$ satisfies the criteria of the ES-VRH conduction, the estimated localization length has unreasonable low value. The Mott insulating ground state in the BSMO system is confirmed from the fact that the AFM ordering takes place in the insulating phase and the resistivity does not show any anomaly at T_N. The resistivity data can be qualitatively analyzed in view of the percolation model, which considers the coexistence of FM and AFM domains in the BSMO system. Similar conclusions are drawn from our earlier temperature dependent ESR and resistivity measurements on $Bi_{(1-x)}Ca_xMnO_3$ [42,43]. The BCMO samples show lower T_{CO} value compared with BSMO samples. The resistivity data for BCMO system shows linear variation of $\ln \rho$ with $T^{-1/2}$ in the CO state. Whereas BSMO system does not follow this temperature variation in CO state for all the compositions. Moreover, the resistivity of BSMO system is about one to two order higher than that of BCMO system.

Acknowledgement

JK acknowledges the financial support from Council of Scientific and Industrial Research (CSIR), India in the form of Research Associateship (RA).

References

[1] S. Jin, T.H. Tiefel, M. McCormack, R.A. Fastnacht, R. Ramesh, L.H. Chen, Science 264 (1994) 413.
[2] G.C. Xiong, Q. Li, H.L. Ju, S.M. Bhagat, S.E. Lofland, R.L. Greene, T. Venkatesan, Appl. Phys. Lett. 67 (1995) 3031.
[3] Y. Tokura, Y. Tomioka, H. Kuwahara, A. Asamitsu, Y. Morimito, M. Kasai, J. Appl. Phys. 79 (1996) 5288.
[4] Z. Jirak, S. Krupicka, Z. Simsa, M. Dlouha, S. Vrastislav, J. Magn. Magn. Mater. 53 (1985) 153.
[5] H. Kuwahara, Y. Tomioka, A. Asamitsu, Y. Moritomo, Y. Tokura, Science 270 (1995) 961.
[6] Y. Tokura, Y. Tomioka, J. Magn. Magn. Mater. 200 (1999) 1.
[7] M.B. Salamon, Rev. Mod. Phys. 73 (2001) 583.
[8] E. Dagotto, Nanoscale Phase Separation and Colossal Magnetoresistance, Springer, Berlin, 2002.
[9] T. Atou, H. Chiba, K. Ohoyama, Y. Yamaguchi, Y. Syono, J. Solid State Chem. 145 (1999) 639.
[10] T. Kimura, S. Kawamoto, I. Yamada, M. Azuma, M. Takano, Y. Tokura, Phys. Rev. B 67 (2003) 180401 (R).
[11] Z. Branković, Z. Marinković Stanojević, L. Mančić, V. Vukotić, S. Bernik, G. Branković, J. Eur. Ceram. Soc. 30 (2010) 277.
[12] N.E. Rajeevan, P.P. Pradyumnan, R. Kumar, D.K. Shukla, S. Kumar, A.K. Singh, S. Patnaik, S.K. Arora, I.V. Shvets, Appl. Phys. Lett. 92 (2008) 102910.
[13] H. Ken-ichi, E. Ohta, H. Wada, H. Higuma, Jpn. J. Appl. Phys. 39 (2000) L1308.
[14] H. Ken-ichi, E. Ohta, H. Wada, H. Higuma, S. Miyashita, Jpn. J. Appl. Phys. 40 (2001) 5281.
[15] N. Kumar, H. Kishan, A. Rao, V.P.S. Awana, J. Alloys Compd. 504 (2010) L39.
[16] L. Beibei, J. Zhiyi, D. Bo, C. Fanglin, X. Changrong, J. Power Sources 196 (2011) 999.
[17] J.L Garcia-Munoz, C. Frontera, M.A.G. Aranda, A. Llobet, C. Ritter, Phys. Rev. B 63 (2001) 064415.
[18] J.L. Garcia-Munoz, C. Frontera, P. Beran, N. Bellido, J.S. Lord, C. Ritter, I. Margiolaki, J. Phys. Condens. Matter 19 (2007) 406212.
[19] J.L. Garcia Munoz, C. Frontera, M.A.G. Aranda, C. Ritter, A. Llobet, M. Respaud, M. Goiran, H. Rakoto, O. Masson, J. Vanacken, J.M. Broto, J. Solid State Chem. 171 (2003) 84.
[20] J.L. Garcia-Munoz, F. Carlos, R. Marc, G. Maud, R. Clemens, X.G. Capdevila, Phys. Rev. B 72 (2005) 054432.
[21] D. Sedmidubsky, O. Bene, P. Beran, J. Hejtmanek, M. Marysko, J. Magn. Magn. Mater. 272–276 (2004) E285.
[22] G. Subias, M.C. Sanchez, J. Garcia, J. Blasco, J. Herrero-Martin, C. Mazzoli, P. Beran, M. Nevriva, J.L. Garcia-Munoz, J. Phys. Condens. Matter 20 (2008) 235211.
[23] D. Sedmidubsky, A. Strejc, O. Benes, K. Ruzicka, J. Hejtmanek, P. Javorsky, M. Nevriva, C. Martin, J. Solid State Chem. 179 (2006) 3798.
[24] O.S. Mantytskaya, I.O. Troyanchuk, A.N. Chobot, H. Szymczak, Low Temp. Phys. 30 (2004) 218.
[25] B.H. Kim, J.S. Kim, M.S. Kim, C.J. Zhamg, K.H. Kim, B.G. Kim, H.C. Kim, Y.W. Park, Phys. Lett. A 351 (2006) 368.
[26] B.H. Kim, J.S. Kim, T.H. Park, S.J. Park, K.H. Kim, G. Bog, Y.W. Park, J. Phys. Condens. Matter 19 (2007) 476203.
[27] A. Rebello, R. Mahendiran, Appl. Phys. Lett. 94 (2009) 112107.
[28] M. Nagao, K. Kimoto, Y. Matsui, Physica B 405 (2010) 1686.
[29] A. Gupta, S.B. Samanta, V.P.S. Awana, H. Kishan, A.M. Awasthi, S. Bhardwaj, A.V. Narlikar, C. Frontera, J.L. Garcia-Munoz, Physica B 370 (2005) 172.
[30] C. Castellano, M. Ferretti, A. Martinelli, M.R. Cimberle, J. Alloys Compd. 478 (2009) 479.
[31] L. Joshi, V. Dayal, N. Rama, S. Keshri, J. Alloys Compd. 479 (2009) 879.
[32] R. Cortés-Gil, J.M. Alonso, J.M. Rojo, A. Hernando, M. Vallet-Regí, M.L. Ruiz-González, J.M. González-Calbet, Prog. Solid State Chem. 38 (2010) 38.
[33] L. Ling, L. Zhang, Z. Zhang, L. Pi, S. Tan, Y. Zhang, Solid State Commun. 150 (2010) 1802.
[34] M. Quintero, J. Sacanell, L. Ghivelder, A.M. Gomes, A.G. Leyva, F. Parisi, Appl. Phys. Lett. 97 (2010) 121916.
[35] R. Mohan, KumarF N., B. Singh, N.K. Gaur, S. Bhattacharya, S. Rayaprol, A. Dogra, S.K. Gupta, S.J. Kim, R.K. Singh, J. Alloys Compd. 508 (2010) L32.
[36] Y. Wang, Y. Sui, X. Wang, Y. Su, W. Su, X. Liu, H. Fan, J. Phys. Chem. C 114 (2010) 1491.
[37] Y. Qin, T.A. Tyson, K. Pranzas, H. Eckerlebe, J. Phys. Condens. Matter 20 (2008) 195209.
[38] D. Tzankov, D. Kovacheva, K. Krezhov, R. Puźniak, A. Wiśniewski, E. Sváb, M. Mikhov, J. Appl. Phys. 103 (2008) 053910.
[39] L.H. Yin, Y.P. Sun, F.H. Zhang, W.B. Wu, X. Luo, X.B. Zhu, Z.R. Yang, J.M. Dai, W.H. Song, R.L. Zhang, J. Alloys Compd. 488 (2009) 254.
[40] R.R. Zhang, G.L. Kuang, B.C. Zhao, Y.P. Sun, Solid State Commun. 150 (2010) 209.
[41] R. Li, Z. Qu, J. Fang, X. Yu, L. Zhang, Y. Zhang, Solid State Commun. 150 (2010) 389.
[42] J. Kurian, R. Singh, J. Appl. Phys. 103 (2008), 07F707.
[43] J. Kurian, R. Singh, J. Phys. D 41 (2008) 215006.
[44] J. Kurian, R. Singh, J. Appl. Phys. 105 (2009) 09D718.
[45] J. Kurian, R. Singh, J. Phys. Conf. Ser. 200 (2010) 012100.
[46] J. Kurian, R. Singh, J. Appl. Phys. 107 (2010) 09D715.
[47] H. Chiba, T. Atou, Y. Syono, J. Solid State Chem. 132 (1997) 139.
[48] K.T. Jacob, K.P. Jayadevan, J. Mater. Res. 13 (1997) 1905.
[49] S.B. Oseroff, M. Torikachvili, J. Singley, S. Ali, S.W. Cheong, S. Schultz, Phys. Rev. B 53 (1996) 6521.
[50] A. Shengelaya, G.M. Zhao, H. Keller, K.A. Muller, Phys. Rev. Lett. 77 (1996) 5296.
[51] H. Chiba, M. Kikuchi, K. Kusaba, Y. Syono, Solid State Commun. 99 (1996) 499.
[52] H. Chiba, T. Atou, H. Faqir, M. Kikuchi, Y. Syono, Y. Murakami, D. Shindo, Solid State Ion. 108 (1998) 193.
[53] A.I. Shames, E. Rozenberg, G. Gorodetsky, J. Pelleg, B.K. Chaudhuri, Solid State Commun. 107 (1998) 91.
[54] A.I. Shames, A. Yakubovsky, V. Amelichev, O. Gorbenko, A. Kaul, Solid State Commun. 121 (2002) 103.
[55] S. Yunoki, J. Hu, A.L. Malvezzi, A. Moreo, N. Furukawa, E. Dagatto, Phys. Rev. Lett. 80 (1998) 845.
[56] M.T. Causa, M. Tovar, A. Caneiro, F. Prado, G. Ibanez, C.A. Ramos, A. Butera, B. Alascio, X. Obradors, S. Pinol, F. Rivadulla, C. Vazquez-Vazquez, M.A. Lopez-Quintela, J. Rivas, Y. Tokura, S.B. Oseroff, Phys. Rev. B 58 (1998) 3233.
[57] C. Frontera, J.L. Garcia-Munoz, M. Angel, G. Aranda, C. Ritter, A. Llobet, M. Respaud, J. Vanacken, Phys. Rev. B 64 (2001) 054401.
[58] T.L. Phan, S.G. Min, M.H. Phan, N.D. Ha, N. Chau, S.C. Yu, Phys. Status Solidi B 244 (2007) 1109.
[59] J.P. Joshi, A.K. Sood, S.V. Bhat, S. Parasharb, A.R. Rajub, C.N.R. Rao, J. Magn. Magn. Mater. 279 (2004) 91.
[60] C. Frontera, J.L. Garcia-Munoz, A. Llobet, M.A.G. Aranda, C. Ritter, M. Respaud, J. Vanacken, J. Phys. Condens. Matter 13 (2001) 1071.
[61] P.V. Vanitha, R.S. Singh, S. Natarajan, C.N.R. Rao, J. Solid State Chem. 137 (1998) 365.

[62] M. Jaime, M.B. Salamon, Phys. Rev. B 54 (1996) 11914.
[63] R. Raffaelle, H.U. Anderson, D.M. Sparlin, P.E. Parris, Phys. Rev. B 43 (1991) 7991.
[64] T. Holstein, Ann. Phys. 21 (1968) 193.
[65] D. Emin, T. Holstein, Ann. Phys. 53 (1969) 439.
[66] I.G. Austin, N.F. Mott, Adv. Phys. 18 (1969) 41.
[67] H. Boettger, V. Bryksin, Hopping Conduction in Solids, Akademic, Berlin, 1985.
[68] N.F. Mott, Conduction in Non-crystalline Materials, Oxford University Press, New York, 1993.
[69] N.F. Mott, E.A. Davis, Electronic Processes in Non Crystalline Materials, Clarendon Press, Oxford, 1971.
[70] H. Boettger, V. Bryksin, Hopping Conduction in Solids, Akademic-Verlag, Berlin, 1985.
[71] P.W. Anderson, Phys. Rev. 109 (1958) 1492.
[72] Q. Li, J. Zang, A.R. Bishop, C.M. Soukoulis, Phys. Rev. B 56 (1997) 4541.
[73] T. Schwartz, G. Bartal, S. Fishman, M. Segev, Nature 446 (2007) 52.
[74] Y. Lahini, A. Avidan, F. Pozzi, M. Sorel, R. Morandotti, D.N. Christodoulides, Y. Silberberg, Phys. Rev. Lett. 100 (2008) 013906.
[75] J. Billy, V. Josse, Z. Zuo, A. Bernard, B. Hambrecht, P. Lugan, D. Clement, S.-P. Laurent, B. Philippe, A. Aspect, Nature 453 (2008) 891.
[76] E. Zacharias, R. Singh, Solid State Commun. 93 (1995) 135.
[77] R. Rosenbaum, N.V. Lien, M.R. Graham, M. Witcomb, J. Phys. Condens. Matter 9 (1997) 6247.
[78] R. Rosenbaum, Phys. Rev. B 44 (1991) 3599.
[79] J.-J. Kim, H. Jong Lee, Phys. Rev. Lett. 70 (1993) 2798.
[80] M. Viret, L. Ranno, J.M.D. Coey, Phys. Rev. B 55 (1997) 8067.
[81] J.L. García-Muñoz, C. Frontera, B. Rivas-Murias, J. Mira, J. Appl. Phys. 105 (2009) 084116.
[82] B.I. Shklovskii, A.L. Efros, Electronic Properties of Doped Semiconductors Springer, Springer, Berlin, Heidelberg, 1984.
[83] A.L. Efros, B.I. Shklovskii, J. Phys. C Solid State Phys. 8 (1975) L49.
[84] C. Krishnamoorthy, K. Sethupathi, V. Sankaranarayanan, R. Nirmala, S.K. Malik, J. Magn. Magn. Mater. 308 (2007) 28.
[85] C.M. Varma, Phys. Rev. B 54 (1996) 7328.
[86] L. Sheng, D.Y. Xing, D.N. Sheng, C.S. Ting, Phys. Rev. Lett. 79 (1997) 1710.
[87] A. Yildiz, S.B. Lisesivdin, M. Kasap, D. Mardare, J. Non-Cryst. Solids 354 (2008) 4944.
[88] S.S.N Bharadwaja, C. Venkatasubramanian, N. Fieldhouse, S. Ashok, M.W. Horn, T.N. Jackson, Appl. Phys. Lett. 94 (2009) 222110.
[89] B.I. Shklovskii, A.L. Efros, Electronic Properties of Doped Semiconductors, Springer, Berlin, 1984, p. 206.
[90] B.I. Shklovskii, A.L. Efros, Electronic Properties of Doped Semiconductors, Springer, Berlin, 1984, p. 240.
[91] A. Matthias Mayr, J.A. Morea, J. Verges, A. Arispe, E. Feiguin, Dagotto, Phys. Rev. Lett. 86 (2001) 135.
[92] C.J. Adkins, J. Phys. Condens. Matter 1 (1989) 1253.
[93] W.N. Shafarman, D.W. Koon, T.G. Castner, Phys. Rev. B 40 (1989) 1216.
[94] T.G. Castner, in: M. Pollak, B.I. Shklovskii (Eds.), Hopping Transport in Solids, Elsevier, North-Holland, Amsterdam, 1990, p. 1.
[95] S. Nakatsuji, V. Dobrosavljevic, D. Tanaskovic, M. Minakata, H. Fukazawa, Y. Maeno, Phys. Rev. Lett. 93 (2004) 146401.